Volume 1 | Number 1 | Jan 2013 | Pages 1–100

Journal of
Materials Chemistry A

Materials for energy and sustainability
www.rsc.org/materialsA

Li⁺

ROYAL SOCIETY
OF CHEMISTRY

This is an *Accepted Manuscript*, which has been through the Royal Society of Chemistry peer review process and has been accepted for publication.

Accepted Manuscripts are published online shortly after acceptance, before technical editing, formatting and proof reading. Using this free service, authors can make their results available to the community, in citable form, before we publish the edited article. We will replace this *Accepted Manuscript* with the edited and formatted *Advance Article* as soon as it is available.

You can find more information about *Accepted Manuscripts* in the **Information for Authors**.

Please note that technical editing may introduce minor changes to the text and/or graphics, which may alter content. The journal's standard **Terms & Conditions** and the **Ethical guidelines** still apply. In no event shall the Royal Society of Chemistry be held responsible for any errors or omissions in this *Accepted Manuscript* or any consequences arising from the use of any information it contains.

Journal of Materials Chemistry

ARTICLE

Enthalpy of Formation and Thermodynamic Insights into Yttrium Doped BaZrO₃

M.D. Gonçalves[a,b], P.S. Maram[a], R. Muccillo[b], A. Navrotsky[a],

The enthalpies of formation from binary oxide components at 25 °C of $Ba(Zr_{1-x}Y_x)O_{3-\delta}$, x = 0.1 to 0.5 solid solutions are measured by high temperature oxide melt solution calorimetry in a molten solvent, $3Na_2O \cdot 4MoO_3$ at 702 °C. The enthalpy of formation is exothermic for all the compositions and becomes less negative when increasing yttrium content from undoped (-115.12 ± 3.69 kJ/mol) to x = 0.5 (-77.09 ± 4.31 kJ/mol). The endothermic contribution to the enthalpy of formation with doping content can be attributed to lattice distortions related to the large ionic radius difference of yttrium and zirconium and vacancy formation. For 0.3 < x < 0.5, the enthalpy of formation appears to level off, consistent with an exothermic contribution from defect clustering. Raman spectra indicate changes in short range structural features as a function of dopant content and, suggests that from x = 0.3 to 0.5 the defects begins to cluster significantly in the solid solution, which corroborates with the thermodynamic data and the drop-off in proton conductivity at x > 0.3.
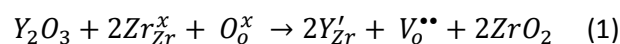
Introduction

The oxide ion conductor yttrium doped barium zirconate (YBZ) has been the focus of several studies during the last decade, mainly due to its chemical stability under CO_2 rich environments and its high proton conductivity at intermediate temperatures[1-3]. Thus, YBZ solid solutions are promising materials for application as solid electrolytes in solid oxide fuel cells (SOFCs) operated at intermediate temperatures (400 – 700 °C)[4]. This operating temperature range could improve the fuel cell lifetime and component compatibility, when compared to high temperature SOFCs (800-1000 °C)[5-7].

Due to its refractory nature (melting point ~2600 °C), downsides of Y-doped barium zirconate are its chemical inhomogeneity, poor densification and grain growth when powders are synthesized by conventional solid state reaction, requiring extreme sintering conditions (1500-1700 °C) and long dwell times. Along with these processing conditions, barium oxide (BaO) volatilization is also a major concern in YBZ[4, 8-10]. Many efforts have been made to improve phase and microstructure homogeneity, densification, grain growth and proton conductivity by using several wet-chemical synthesis methods, co-doping, and different sintering strategies[11-20]. So far, the composition with 20 mole % yttrium content ($BaZr_{0.8}Y_{0.2}O_{3-\delta}$) achieves maximum proton conductivity among YBZ solid solutions, namely greater than 1×10^{-2} S/cm at 450 °C, under optimized processing conditions[3, 16, 21]. The decrease of proton conductivity for YBZ compositions containing more than 20 mole % of Yttrium are related with the reduced symmetry due to lattice distortions, increased oxygen basicity (Y^{3+} is less electronegative than Zr^{4+}) and proton trapping effects due to the formation of dopant-defect associates which reduce the mobility of charge carriers[21-27].

Recently, attention has turned to the complex defect chemistry of yttrium-doped barium zirconate, since it plays an important role in the understanding of proton conductivity[28]. YBZ has a perovskite structure, ABO_3, which is ideally cubic where the A-site is usually occupied by a divalent cation (A= Ba, Pb, Ca) and the B-site by a tetravalent cation (B = Zr, Ce, Ti), with coordination numbers of 12 and 6, respectively[29, 30]. As described, the structure does not include protons, and for their incorporation the perovskite host matrix has to be doped by a trivalent cation on the B-site which will create oxygen vacancies ($V_o^{\bullet\bullet}$) as charge compensating defects. Upon exposure to humid atmosphere, water molecule will dissociate into a hydroxyl group and a proton, which will fill an oxygen vacancy and bond to a lattice oxygen (O_o^x), respectively[15, 25, 31]. These two steps are respectively illustrated by the reactions 1 and 2, written by Kröger-Vink notation:

$$Y_2O_3 + 2Zr_{Zr}^x + O_o^x \rightarrow 2Y_{Zr}' + V_o^{\bullet\bullet} + 2ZrO_2 \quad (1)$$

$$H_2O_g + V_o^{\bullet\bullet} + O_o^x \leftrightarrow 2OH_o^{\bullet} \quad (2)$$

The creation of defects in the structure depends on the nature of the dopant and its concentration[32, 33]. These defects

affect the thermodynamic stability, water uptake and proton mobility. Investigations of defect chemistry of Y-doped barium zirconate have been done by several methods such as density functional theory (DFT)[28, 34], impedance spectroscopy (IS)[3, 35], Raman spectroscopy[36, 37], water uptake by thermogravimetric analysis (TG)[15, 38], and X-ray absorption fine structure (XAFS) spectroscopy[16]. A powerful method to give valuable information about the defect chemistry of solid oxides is the measurement of the formation enthalpy as a function of the dopant concentration by high temperature oxide melt solution calorimetry[39]. Previous works using this technique on ceria and thoria based fluorite structures correlates the enthalpy of formation with the conductivity behaviour of these compounds[40-44]. It was found that the conductivity will reach its maximum when the dopant concentration does not exceed its dilute regime (critical concentration) in the host matrix. Above the critical concentration vacancy clustering is likely to occur, which immobilizes some of the vacancies needed for conduction.

The present work describes the first measurement of the enthalpy of formation of yttrium-doped barium zirconate with Y content (Y/(Y+Zr)) ranging from 10 to 50 mole %. The thermodynamic data give insights about YBZ defect chemistry which will affect both oxide ion conductivity and the incorporation of H_2O for proton conductivity.

Experimental Procedure

Synthesis of yttrium doped barium zirconate powders

Barium zirconate ($BaZrO_3$) and yttrium-doped barium zirconate compositions ($BaZr_{1-x}Y_xO_{3-\delta}$), (x = 0.1 to 0.6), referred to as BZ and YBZx (x in mol %), were synthesized by the oxidant-peroxo method (OPM)[18, 45, 46]. To avoid contamination by atmospheric carbon dioxide, the synthesis was performed in a glove box under nitrogen and used deionized water previously degassed by bubbling with nitrogen gas. The starting materials were barium nitrate (99.9 % $Ba(NO_3)_2$, Alfa Aesar), hydrated yttrium nitrate (99.999 %, $Y(NO_3)_3.xH_2O$ Alfa Aesar) and hydrated zirconyl (IV) nitrate (99.99 %, $ZrO(NO_3)_2.2H_2O$ Alfa Aesar). The molar quantity of Y^{3+} and Zr^{4+} ions per gram of the respective hydrated reagent was determined by gravimetric analysis, at 900 °C for 4 h. For the synthesis, $ZrO(NO_3)_2.2H_2O$ was added into 50 mL of hydrogen peroxide (35 % H_2O_2, AR) to obtain the soluble zirconium peroxo-complex ($ZrO(O_2)H^+$). $Y(NO_3)_3.xH_2O$ and $Ba(NO_3)_2$ were dissolved in 100 mL of deionized water. The solutions were mixed and homogenized for 30 min. The aqueous metal nitrate solution was added into an oxidant mixture (pH = 11) of 50 mL of hydrogen peroxide and 80 mL of aqueous ammonia solution (NH_4OH 28-30 %, Sigma Aldrich) under stirring. The resultant precipitate was stirred for 1 h, filtered and washed with deionized and degassed water and ethanol. The powder was dried at room temperature in a vacuum chamber overnight and ground in an agate mortar. The powder obtained at this step is to as the "precursor". Samples of

each precursor composition were annealed at 1200 °C for 24 h to obtain the bulk crystalline phase. Figure 1 illustrates the flow chart of the experimental procedure.
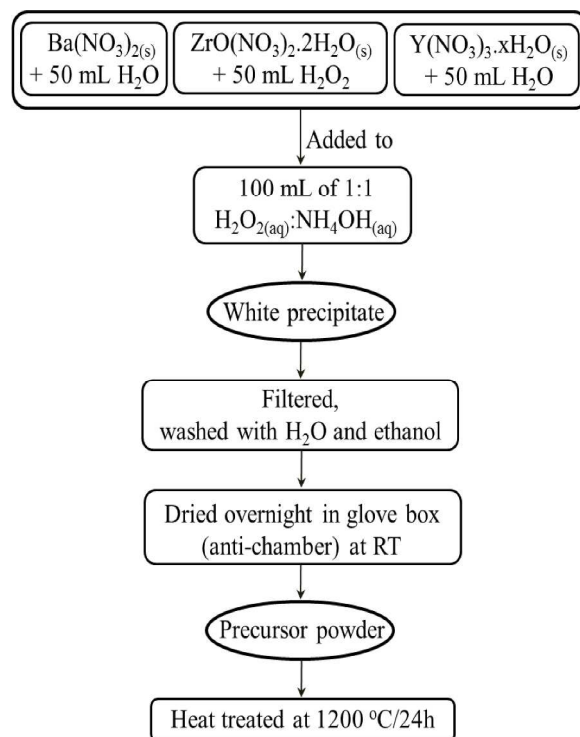

Figure 1 – Flow chart of the oxidant-peroxo method approach for synthesis of $Ba(Zr_{1-x}Y_x)O_{3-\delta}$, with x= 0 to 0.6, compositions.

Characterization

All the synthesized compositions were analysed by powder X-ray diffraction (XRD) measurements using a Bruker AXS D8 Advance diffractometer (Bruker, Madison, WI) operated with CuKα radiation. Data were collected in the 2θ range from 20 to 80 °, with a step size of 0.02 ° and collection time of 1 s/step. The data analysis software Jade 6.1 (Materials Data Inc, Livermore, CA) was used for phase identification. The lattice parameters were evaluated with UnitCell software and are given in Table 1.

Laser Raman spectra were recorded at room temperature for all the solid solutions with a Renishaw RM1000 system integrated with Leica DMLM microscope with a motorized stage using argon ion laser (514.5 nm) operating at 9A and 20 mW. The Raman shifts was calibrated with a standard silicon film.

Quantitative chemical analysis was performed using a wavelength dispersive spectrometer Cameca SX-100 electron microprobe operated at an accelerating voltage of 15 kV, probe current of 20 nA and beam size of 1 μm. For this purpose the heat treated powder samples were pressed into 5 mm diameter pellets and sintered at 1200 °C for 24 h, polished and carbon-coated. The composition of each sample was determined using an average of 6 - 10 points. For qualitative analysis of sample

homogeneity, backscattered electron images and X-ray dot maps were collected.

Calorimetry

High-temperature oxide melt drop solution calorimetry was performed in a custom built, isoperibol Tian-Calvet twin microcalorimeter maintained at 702 °C as described previously[47-49]. Calibration was done against the known heat content of α-alumina (Alfa Aesar, 99.997 %)[47]. Molten sodium molybdate ($3Na_2O \cdot 4MoO_3$) was the solvent. The glassware assembly was also flushed with oxygen at 40 mL/min to purge any possible gases (H_2O and CO_2) evolved during the experiment and oxygen was also bubbled through the solvent at 4.5 mL/min to maintain oxidizing conditions and stir the melt to aid dissolution. About 5 mg of the sample was loosely pressed into a pellet, and dropped from room temperature into 20 g of the molten solvent in the calorimeter at 702 °C. ZrO_2 and Y_2O_3 measured previously[48,47], were used as reference binary oxides but, since BaO is hygroscopic and difficult to handle because of its instability to CO_2, we used barium carbonate ($BaCO_3$, 99.9 %, Alfa Aesar). Before the calorimetric experiment, the $BaCO_3$ was heated at 800 °C for 1 h to decompose any barium hydroxide impurities. The drop solution enthalpy for BaO is calculated based on the thermochemical cycle in Table 2. The measured heat of drop solution (ΔH_{ds}) was obtained as the average of 8-12 drops to achieve statistically reliable data and the uncertainties were calculated as twice the standard deviation of the mean. The enthalpy of formation for BZ and YBZ10-50 solid solutions from their binary oxides (ΔH_{fox}) were calculated using the drop solution enthalpies. The thermodynamic cycles used for the calculation are given in Table 3.

Results

Figure 2 illustrates the XRD patterns of undoped $BaZrO_3$ and YBZ10-60 powders after heat treatment at 1200 °C for 24 h. The cubic perovskite phase was indexed (PDF #06-0399, a = 4.1973 Å) for all samples. A secondary phase was identified only for YBZ60 and the peaks were indexed as yttrium oxide (PDF #41-1105). As the yttrium content increases, the diffraction peaks shift to lower angles indicating the expansion of the lattice.

Table 1 summarizes the nominal and WDS analysed composition for all the YBZx samples. The nominal Zr/Y molar ratios and those determined by WDS are the same within experimental error for samples with x = 0 to x = 0.5. The microprobe analysis also suggests some barium loss with increasing dopant concentration, which was expected to occur due to the long annealing time of samples and creation of charge compensating defects[50]. It is already known that the YBZ cubic perovskite structure can accommodate a Ba deficiency up to $Ba_{0.93}Zr_{1-x}Y_xO_{3-\delta}$ and still be in single-phase [16, 38]. Yttrium solubility in BZ ranges from x = 0.3 in

stoichiometric and x = 0.5 in Ba non-stoichiometric samples[16, 38, 51, 52]. These observations are consistent with the absence of secondary phases in the YBZ10-50 samples.
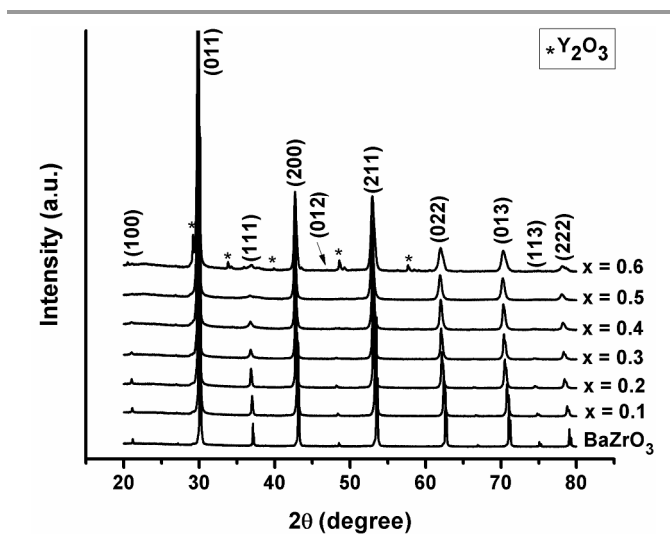

Figure 2 – Powder X-ray diffraction patterns of YBZx with different Y content (0 ≤ x ≤ 0.6). The powder samples had been heat treated at 1200 °C for 24 h. Secondary phase of Y_2O_3 was identified at sample YBZ60.

Table 1 – Chemical analysis and lattice parameter of YBZ solid solutions heat treated at 1200 °C for 24h.

Nominal Composition	Stoichiometry by microprobe analysis			Lattice Parameter (Å)
	Y	Zr	Ba	
$BaZrO_3$		1.004(5)	0.992 (10)	4.193(1)
$Ba(Zr_{0.9}Y_{0.1})O_{2.95}$	0.099 (3)	0.908(4)	0.986 (5)	4.205(1)
$Ba(Zr_{0.8}Y_{0.2})O_{2.90}$	0.203 (4)	0.807(4)	0.982 (4)	4.221(1)
$Ba(Zr_{0.7}Y_{0.3})O_{2.85}$	0.309 (6)	0.718(8)	0.951 (8)	4.227(1)
$Ba(Zr_{0.6}Y_{0.4})O_{2.80}$	0.409 (10)	0.614 (12)	0.952 (11)	4.232(1)
$Ba(Zr_{0.5}Y_{0.5})O_{2.75}$	0.524 (11)	0.518 (6)	0.989 (8)	4.237(1)
$Ba(Zr_{0.4}Y_{0.6})O_{2.70}$	0.676 (21)	0.428 (14)	0.823 (34)	4.232(7)

*The figures in parentheses refer to the least significant digits

The lattice parameters of the YBZx powders (Table 1) are in general agreement with the literature despite the wide range of values reported, which can be attributed to composition deviation from the stoichiometric solid solution[38, 50, 53-56].

The Goldschmidt tolerance factor (t)[57] was calculated using equation 3 to predict the stability of the cubic structure with the variation of the dopant content

$$t = \frac{(r_A + r_O)}{\sqrt{2}(r_B + r_O)} \qquad (3)$$

where r_A and r_B are respectively the ionic radii of the cations which occupy the A and B sites of the perovskites and r_O is the ionic radii for the oxygen anion[58]. Figure 3 illustrates the values
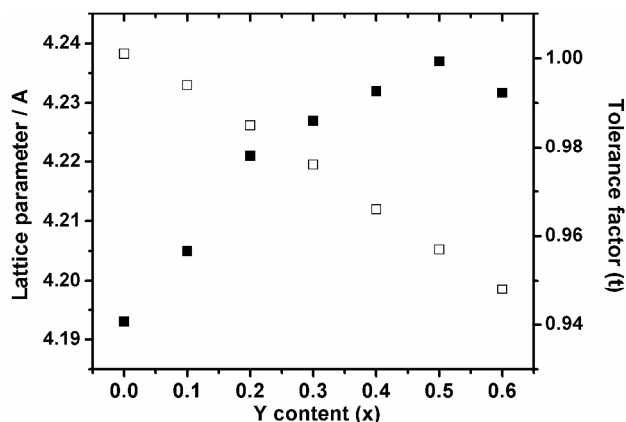

Figure 3- Calculated lattice parameters (left axis, solid squares) and tolerance factor (*t*) (right axis, open squares) of YBZx as a function of yttrium concentration, x.

for the ideal BZ and YBZ10-60 solid solutions compared to the measured lattice parameters (Table 1). As the yttrium content increases, the lattice parameters increase and the tolerance factor deviates more from unity. Ideally, the lattice parameters would increase linearly since the Zr^{4+} cation is partially substituted by the larger Y^{3+} cation ($R_{Zr^{4+}} = 0.72$ Å; $R_{Y^{3+}} = 0.90$ Å[58]). However, the slope of the lattice parameter curve changes at x = 0.3, which may be related to increasing Ba loss (Table 1). The tolerance factor for the ideal YBZ60 (t = 0.948) suggests that the formation of a phase with cubic symmetry may not be favored since the range for the stability of the cubic perovskite structure is generally given as $0.95 \leq t \leq 1.04$[59]. The YBZ60 sample exceeds the yttrium solubility limit, as shown the secondary phase in its XRD pattern (Figure 2). No further experiments were carried out with the YBZ60 sample.

Figure 4 illustrates the Raman spectra of YBZ solid solutions as a function of dopant content. The Raman spectrum of ideal cubic perovskite is expected to be featureless, but several vibrational modes were observed for all samples. In the case of barium zirconate, with neither dopant atoms nor oxygen vacancies, the observation of active vibrational modes was attributed to second order scattering[60, 61]. However, Karlsson et al. suggested that the presence of the band around 200 cm^{-1}, related to torsional motion of the lattice, supports that the spectrum originates from lattice distortions[62]. Slodczyk et al, suggested that the active BZ Raman spectrum is indicative of nanodomains with local symmetry different from that of the cubic structure[63], although, since the spectra consist of broad bands these distortions are expected to be small[62].

Essentially, most of the bands appear in all samples, with some shifting or differing in intensity with composition. The motions of the Ba^{2+} network, dominated by Coulombic

interactions, will give rise to the translation oscillation modes from 50 to 250 cm^{-1} [62-64]. The peaks at higher frequencies are usually assigned to modes of the more covalently bonded oxygen octahedra[37, 61-63]. More specifically, the peaks in the regions 300 – 500 and 600 – 900 cm^{-1} can be assigned to bending (δ) and symmetric stretching (v) of oxygen bonds[63, 64].
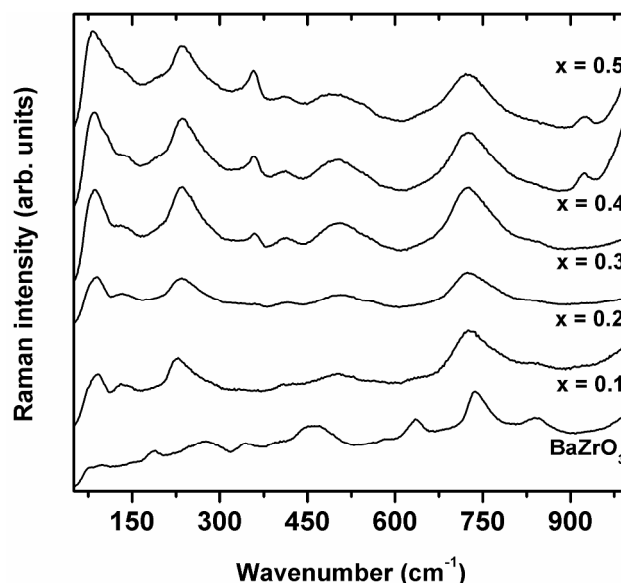

Figure 4- Raman spectra of BaZrO$_3$ and Ba(Zr$_{1-x}$Y$_x$)O$_{3-\delta}$ (0 ≤ x ≤ 0.5) samples.
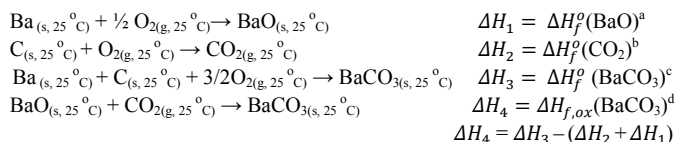
In the doped compositions the distortions are mainly related to changes in the BO$_6$ octahedra (250 to 900 cm^{-1}) due to accommodation of larger Y^{3+} atoms at the B-site and the creation of oxygen vacancies, which will lead to a tilt of the octahedra and a slight distortion along the c-axis[35, 36, 61-63]. The bands below 200 cm^{-1} shift to lower wavenumbers and become more intense with increasing dopant content. The vibrations around 90-120 and 130 cm^{-1} are respectively assigned to deformational motions and stretching vibrations of the Ba-[(Zr/Y)]O$_6$[62]. These two bands are indicators of the structure of the solid solution and are consistent with a cubic perovskite without structural phase transition[62]. Their increased intensity and broadening when Y concentration increases can be related to the observed barium deficiency and the possibility of Y siting at the A-site, since the force constant of Y[(Zr/Y)]O$_6$ is expected to be lower than that of Ba-[(Zr/Y)]O$_6$. The peaks near 230-300, 400 and 750 cm^{-1} become more intense with increasing dopant content except for the sample with x = 0.2 which has less intense and broad peaks. The bands around 350 and 430-550 cm^{-1} that occur for BaZrO$_3$ decrease in intensity for x = 0.1 and 0.2 but increase again for x > 0.3. The bands at 636 cm^{-1} and 840 cm^{-1} in BaZrO$_3$ lose intensity and shift to slightly higher wavenumbers when the YO$_6$ octahedra contribution increases with increasing dopant content. The band around 920 cm^{-1} is present as a small shoulder in all samples but increases strongly in intensity for x = 0.4 and 0.5.

With increasing Y concentration local distortions become more pronounced, but without changing the overall aspect of the spectra, which means that the long-range average structure

remains the same as that suggested by the XRD patterns (Figure 2). The distortions of the undoped and doped solid solutions are different, which can be identified by the negative shift of the mode near to 250-350 cm^{-1} from x = 0 to x = 0.1 and is indicative of the changing BO_6 tilt angle.

Tables 2a and 2b show the thermodynamic cycles used for the calculation of BaO drop solution enthalpy from $BaCO_3$ drop solution calorimetry, formation enthalpies from elements, and previously determined CO_2 heat content[65]. The drop solution enthalpy obtained for BaO in this work is -185.30 ± 3.12 kJ/mol, which is consistent with the previous work (-184.61 ± 3.31 kJ/mol[40]), and was used to calculate the formation enthalpy of YBZ solid solutions. Table 3 shows the thermochemical cycle used for the calculation of $Ba_wZr_{1-x}Y_xO_{3-\delta}$ enthalpy of formation at 25 °C from its binary oxides (ΔH_{fox}).

Table 2a - Thermochemical cycle used for calculation of formation enthalpy of $BaCO_3$ from oxides at room temperature.

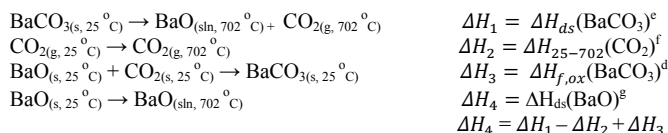$$Ba_{(s, 25\ ^oC)} + \tfrac{1}{2} O_{2(g, 25\ ^oC)} \rightarrow BaO_{(s, 25\ ^oC)} \qquad \Delta H_1 = \Delta H_f^o(BaO)^a$$
$$C_{(s, 25\ ^oC)} + O_{2(g, 25\ ^oC)} \rightarrow CO_{2(g, 25\ ^oC)} \qquad \Delta H_2 = \Delta H_f^o(CO_2)^b$$
$$Ba_{(s, 25\ ^oC)} + C_{(s, 25\ ^oC)} + 3/2 O_{2(g, 25\ ^oC)} \rightarrow BaCO_{3(s, 25\ ^oC)} \quad \Delta H_3 = \Delta H_f^o(BaCO_3)^c$$
$$BaO_{(s, 25\ ^oC)} + CO_{2(g, 25\ ^oC)} \rightarrow BaCO_{3(s, 25\ ^oC)} \quad \Delta H_4 = \Delta H_{f,ox}(BaCO_3)^d$$
$$\Delta H_4 = \Delta H_3 - (\Delta H_2 + \Delta H_1)$$

s = solid; g = gas.

[a] -548.1 ± 2.1 kJ/mol[65].

[b] -393.5 ± 0.1 kJ/mol, enthalpy of formation of CO_2[65].

[c] -1210.90 ± 2.2 kJ/mol, enthalpy of formation from elements[65].

[d] -269.30 ± 3.04 kJ/mol.

Table 2b - Thermochemical cycle used for the calculation of barium oxide enthalpy of drop solution ($\Delta H_{ds}BaO$) from 25 to 702 °C. Solvent: molten $3Na_2O\cdot4MoO_3$ at 975 K.

$$BaCO_{3(s, 25\ ^oC)} \rightarrow BaO_{(sln, 702\ ^oC)} + CO_{2(g, 702\ ^oC)} \quad \Delta H_1 = \Delta H_{ds}(BaCO_3)^e$$
$$CO_{2(g, 25\ ^oC)} \rightarrow CO_{2(g, 702\ ^oC)} \qquad \Delta H_2 = \Delta H_{25-702}(CO_2)^f$$
$$BaO_{(s, 25\ ^oC)} + CO_{2(s, 25\ ^oC)} \rightarrow BaCO_{3(s, 25\ ^oC)} \quad \Delta H_3 = \Delta H_{f,ox}(BaCO_3)^d$$
$$BaO_{(s, 25\ ^oC)} \rightarrow BaO_{(sln, 702\ ^oC)} \qquad \Delta H_4 = \Delta H_{ds}(BaO)^g$$
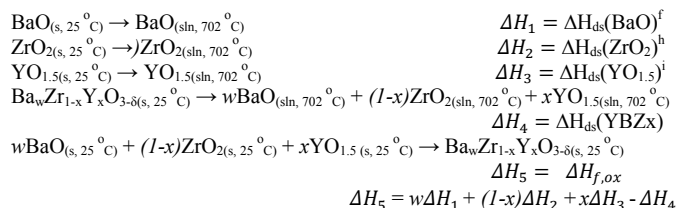$$\Delta H_4 = \Delta H_1 - \Delta H_2 + \Delta H_3$$

s = solid; g = gas; sln = solution.

[e] 116.11 ± 0.69 kJ/mol (this work).

[f] 32.11 kJ/mol, heat content of CO_2 from 25 to 702 °C[65]

[g] -185.30 ± 3.12 kJ/mol.

Table 3 - Thermochemical cycle used for the calculation of $Ba_wZr_{1-x}Y_xO_{3-\delta}$ (bulk) enthalpy of formation at 25 °C ($\Delta H_{f,ox}$) from its binary oxides. Solvent: molten $3Na_2O\cdot4MoO_3$ at 702 °C.

$$BaO_{(s, 25\ ^oC)} \rightarrow BaO_{(sln, 702\ ^oC)} \qquad \Delta H_1 = \Delta H_{ds}(BaO)^f$$
$$ZrO_{2(s, 25\ ^oC)} \rightarrow ZrO_{2(sln, 702\ ^oC)} \qquad \Delta H_2 = \Delta H_{ds}(ZrO_2)^h$$
$$YO_{1.5(s, 25\ ^oC)} \rightarrow YO_{1.5(sln, 702\ ^oC)} \qquad \Delta H_3 = \Delta H_{ds}(YO_{1.5})^i$$
$$Ba_wZr_{1-x}Y_xO_{3-\delta(s, 25\ ^oC)} \rightarrow wBaO_{(sln, 702\ ^oC)} + (1-x)ZrO_{2(sln, 702\ ^oC)} + xYO_{1.5(sln, 702\ ^oC)}$$
$$\Delta H_4 = \Delta H_{ds}(YBZx)$$
$$wBaO_{(s, 25\ ^oC)} + (1-x)ZrO_{2(s, 25\ ^oC)} + xYO_{1.5\ (s, 25\ ^oC)} \rightarrow Ba_wZr_{1-x}Y_xO_{3-\delta(s, 25\ ^oC)}$$
$$\Delta H_5 = \Delta H_{f,ox}$$
$$\Delta H_5 = w\Delta H_1 + (1-x)\Delta H_2 + x\Delta H_3 - \Delta H_4$$

s = solid; sln = solution; Compositions corrected by WDS analysis (Table 1) and are indicated by w, 1-x, x/2 for Ba, Zr and Y respectively; The uncertainties were calculated as two standard deviation of the mean.

[h] 19.5 ± 0.9 kJ/mol[66].

[i] -120.07 ± 2.5 kJ/mol[67].

Table 4 shows the average enthalpy of drop solutions and the enthalpy of formation obtained for each BZ and YBZx composition. The enthalpy of formation of $BaZrO_3$ was previously determined by drop solution calorimetry at 825 °C using an alkali borate solvent (-123.9 ± 4.1 kJ/mol)[68]. The new value is considered more accurate because dissolution of both $BaZrO_3$ and ZrO_2 in alkali borate was somewhat slow and gas bubbling was not used to stir that rather viscous melt.

Table 4- Summary of average ΔH_{ds} data obtained from drop solution calorimetry and used for calculation of the enthalpy of formation of $Ba(Zr_{1-x}Y_x)O_{3-\delta}$ ($0 \le x \le 0.5$) solid solutions.

Nominal Composition	ΔH_{ds} (kJ/mol)	$\Delta H_{f,ox}$ (kJ/mol)
$BaZrO_3$	-49.11(12) ± 1.09	-115.12 ± 3.69
$Ba(Zr_{0.9}Y_{0.1})O_{2.95}$	-64.60 (8) ± 1.49	-106.23 ± 3.65
$Ba(Zr_{0.8}Y_{0.2})O_{2.90}$	-85.53 (11) ± 1.96	-92.84 ± 3.87
$Ba(Zr_{0.7}Y_{0.3})O_{2.85}$	-101.86 (12) ± 1.49	-78.82 ± 3.88
$Ba(Zr_{0.6}Y_{0.4})O_{2.80}$	-111.83 (12) ± 1.61	-76.78 ± 4.63
$Ba(Zr_{0.5}Y_{0.5})O_{2.75}$	-126.97 (12) ± 1.74	-77.09 ± 4.31

Average values from the number of experiments given in parentheses; uncertainties calculated as two standard deviations of the mean.

Figure 5 illustrates the behavior of the drop solution and formation enthalpies as a function of dopant concentration. ΔH_{ds} for all compositions is exothermic and becomes more negative with increasing yttrium content. The calculated $\Delta H_{f,ox}$ is strongly exothermic for all compositions, which means thermodynamic stability with respect to their binary oxides[40,69]. The enthalpy of formation becomes less exothermic with increase of dopant content but for x > 0.3 the values remain the same within experimental error. Interestingly, this observed behavior follows a trend similar to that of proton conductivity, which reaches a maximum for YBZ20 (critical concentration; conductivity ~1.10^{-2} S/cm at 450 °C) and decreases for higher Y content[3, 16, 50].
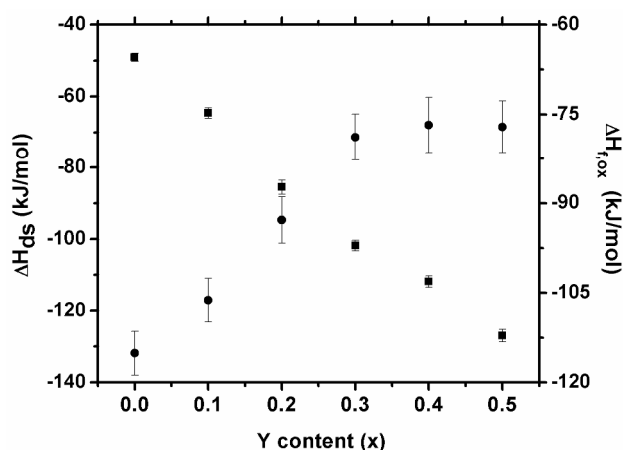
Figure 5 – Enthalpies of drop solution (left, solid squares) and formation from the oxides at 25 °C (right, solid circles) as a function of yttrium content in BZ and YBZx solid solutions, x. The experimental uncertainties are indicated.

Discussion

The enthalpy of formation of YBZ solid solutions can be correlated with the change in its structure and defect chemistry. The tolerance factor deviates linearly from unity as the dopant concentration increases and the thermodynamic stability is expected to decrease[10, 40, 50, 68, 70]. The formation enthalpies from constituent binary oxides indeed show that the energetic stability of the YBZ solid solutions decreases as the Y content increases. Therefore when increasing the Yttrium content, the endothermic increment to the ΔH_{fox} can be attributed to the lattice distortions which occurs in response to size mismatch between cations in the lattice and the formation of oxygen vacancies (equation 1)[42, 44]. Besides this effect, increasing of Y content induced barium loss, more pronounced at x > 0.3. Commonly, the barium loss is attributed to the processing conditions, such as high temperatures and longer dwell times[8, 71], but when increasing the dopant concentration it is also favored[33]. The latter has been related to the dopant partitioning among both A and B sites of the perovskite, which means that yttrium would have an amphoteric character (donor and acceptor) in order to charge balance the structure when barium deficiency occurs. Nonetheless, some authors could not prove that Y partitioning occurs when doping BZ, but showed that it occurs when dopant ionic radii is much larger than that host cation of B-site, for example in BaZrO$_3$ (Gd, Sm, Eu)[15, 32, 33] and also in other perovskite-based oxides, such as BaCeO$_3$, BaTiO$_3$, CaZrO$_3$[26, 72-75]. The implication of the partitioning effect is that yttrium atoms can also occupy the A-site, although oxygen vacancies are consumed and Ba atoms expelled, according to equation 4 below[16, 38, 50].

$$2Ba_{Ba}^{x} + V_{O}^{\bullet\bullet} + Y_2O_3 \rightarrow 2Y_{Ba}^{\bullet} + O_{O}^{x} + 2BaO\uparrow \quad (4)$$
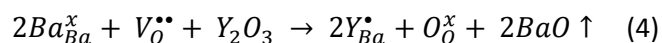
In addition, the decreasing thermodynamic stability of the perovskite with increasing x itself implies a higher BaO activity and a greater thermodynamic driving force for Ba vaporization. Measurements by high temperature oxide melt solution calorimetry on ceria and thoria based fluorite structures have already detected exothermic vacancy clustering when the dopant concentration is above the dilute regime[40-44]. For yttrium-doped barium zirconate, Y partitioning and the defect clustering effects have already been considered from impedance spectroscopy measurements and from calculation of the pre-exponential factor and activation energy[33, 50]. Despite the higher proton concentration with increasing dopant content (equation 2), above x = 0.2, both kinds of defects were suggested to be related to the decrease of the pre-exponential factor and the increase of activation energy, hence decreasing proton conductivity[15, 26, 50, 76]. The present thermochemical data can not distinguish these various factors but are consistent with the observed trends in conductivity. The decrease in peak intensity in our Raman data with increasing dopant concentration up to x = 0.2 may imply increasing short range order on a local scale with strain accommodated in the vicinity of the dopant site. However, above x = 0.3, the Raman bands become more intense, which may suggest that local structural distortions around doped sites have spread throughout the entire structure[62]. Therefore, defect clustering could be enhanced since the high dopant concentration might lead to the formation of different chemical environments not favored when the dopant is in a dilute regime[28]. Although the defect chemistry of these compositions is still not completely elucidated, it appears that for x > 0.3 there is a balance between the exothermic vacancy clustering and Y siting on the perovskite A-site and the endothermic effect of oxygen vacancy formation, lattice distortions, and barium loss. The net effect is a nearly constant enthalpy of formation for 0.3 < x < 0.5. Such clustering, presumably diminishes both oxide ion and proton conductivity and, indeed, the maximum proton conductivity occurs near the dopant concentration (30 mole %) at which the energetics level off and clustering becomes pronounced.

Conclusions

The enthalpy of formation of Y-doped BaZrO$_3$ solid solutions, with increasing Y content was measured by high temperature oxide melt solution calorimetry. The increase of the dopant content causes the destabilization of the perovskite structure due to lattice distortions and formation of oxygen vacancies. The formation enthalpy data also give thermodynamic evidence that dopant-vacancy association and defect clustering may occur when the dopant concentration approaches 30 mole %, which can be related with the trend of the decrease in the proton conductivity.

Acknowledgements

Notes and references

[a] Peter A. Rock Thermochemistry Laboratory and NEAT ORU, University of California, Davis, CA 95516, USA
[b] Cen Center of Science and Technology of Materials, Energy and Nuclear Research Institute, Travessa R 400, Cidade Universitária, S. Paulo, SP 05508-900, Brazil
* Corresponding authors: muccillo@usp.br and anavrotsky@ucdavis.edu

1. Y. Guo, R. Ran and Z. Shao, *Int. J. Hydrogen Energy*, 2011, **36**, 1683-1691.
2. A. Slodczyk, P. Colomban, D. Lamago, G. André, O. Zaafrani, O. Lacroix, A. Sirat, F. Grasset and B. Sala, *J. Mater. Res.*, 2012, **27**, 1939-1949.
3. Y. Yamazaki, R. Hernandez-Sanchez and S. M. Haile, *Chem. Mater.*, 2009, **21**, 2755-2762.
4. R. Cervera, Y. Oyama and S. Yamaguchi, *Solid State Ionics*, 2007, **178**, 569-574.
5. S. M. Haile, *Acta Mater.*, 2003, **51**, 5981-6000.
6. A. Orera and P. R. Slater, *Chemistry of Materials*, 2010, **22**, 675-690.
7. H. Ding, J. Ge and X. Xue, *Electrochem. Solid-State Lett.*, 2012, **15**, B86.
8. F. Iguchi, T. Yamada, N. Sata, T. Tsurui and H. Yugami, *Solid State Ionics*, 2006, **177**, 2381-2384.
9. P. Babilo, T. Uda and S. M. Haile, *J. Mater. Res.*, 2007, **22**, 1322-1330.
10. G. C. C. Costa, P. Saradhi Maram, A. Navrotsky and T. Vanderah, *J. Am. Ceram. Soc.*, 2012, **95**, 3254-3262.
11. S. B. C. Duval, P. Holtappels, U. F. Vogt, U. Stimming and T. Graule, *Fuel Cells*, 2009, **9**, 613-621.
12. P. I. Dahl, H. L. Lein, Y. Yu, J. Tolchard, T. Grande, M.-A. Einarsrud, C. Kjølseth, T. Norby and R. Haugsrud, *Solid State Ionics*, 2011, **182**, 32-40.
13. P. Babilo and S. M. Haile, *J. Am. Ceram. Soc.*, 2005, **88**, 2362-2368.
14. A. Magrez, *Solid State Ionics*, 2004, **175**, 585-588.
15. Y. Yamazaki, P. Babilo and S. M. Haile, *Chem. Mater.*, 2008, **20**, 6352-6357.
16. Y. Yamazaki, R. Hernandez-Sanchez and S. M. Haile, *J. Mater. Chem.*, 2010, **20**, 8158.
17. B. Bendjeriou-Sedjerari, J. Loricourt, D. Goeuriot and P. Goeuriot, *J. Alloys Compd.*, 2011, **509**, 6175-6183.
18. M. D. Gonçalves and R. Muccillo, *Ceram. Int.*, 2014, **40**, 911-917.
19. N. Ito, H. Matsumoto, Y. Kawasaki, S. Okada and T. Ishihara, *Solid State Ionics*, 2008, **179**, 324-329.
20. E. N. S. Muccillo, M. D. Gonçalves, R. L. Grosso and R. Muccillo, *Materials Science Forum*, 2014, **798-799**, 407-412.
21. Y. Yamazaki, F. Blanc, Y. Okuyama, L. Buannic, J. C. Lucio-Vega, C. P. Grey and S. M. Haile, *Nat Mater*, 2013, **12**, 647-651.
22. K. D. Kreuer, *Solid State Ionics*, 1999, **125**, 18.
23. M. S. Islam, R. A. Davies and J. D. Gale, *Chem. Mater.*, 2001, **13**, 7.
24. R. Hempelmann, C. Karmonik, T. Matzke, M. Cappadonia, U. Stimming, T. Springer and M. A. Adams, *Solid State Ionics*, 1995, **77**, 152-156.
25. K. D. Kreuer, *Solid State Ionics*, 1997, **97**, 1-15.
26. R. A. Davies, M. S. Islam and J. D. Gale, *Solid State Ionics*, 1999, **126**.
27. K. D. Kreuer, *Annual Review of Materials Research*, 2003, **33**, 333-359.
28. D. Z. Sahraoui and T. Mineva, *Solid State Ionics*, 2013, **232**, 1-12.
29. T. Ishihara, *Bull.Chem. Soc. Japan*, 2006, **79**, 1155-1166.
30. M. Gazda, P. Jasinski, B. Kusz, B. Bochentyn, K. Gdula-Kasica, T. Lendze, W. Lewandowska-Iwaniak, A. Mielewczyk-Gryn and S. Molin, *Solid State Phenomena*, 2011, **183**, 65-70.
31. F. Giannici, A. Longo, F. Deganello, A. Balerna, A. Arico and A. Martorana, *Solid State Ionics*, 2007, **178**, 587-591.
32. D. Han, Y. Nose, K. Shinoda and T. Uda, *Solid State Ionics*, 2012, **213**, 2-7.
33. S. Imashuku, T. Uda, Y. Nose, G. Taniguchi, Y. Ito and Y. Awakura, *J. Electrochem. Soc.*, 2009, **156**, B1.
34. J.-H. Yang, D.-H. Kim, B.-K. Kim and Y.-C. Kim, *Solid State Ionics*, 2013, **252**, 126-131.
35. K. D. Kreuer, S. Adams, W. Münch, A. Fuchs, U. Klock and J. Maier, *Solid State Ionics*, 2001, **145**, 2001.
36. F. Giannici, M. Shirpour, A. Longo, A. Martorana, R. Merkle and J. Maier, *Chem. Mater.*, 2011, **23**, 2994-3002.
37. M. Karlsson, I. Ahmed, A. Matic and S. G. Eriksson, *Solid State Ionics*, 2010, **181**, 126-129.
38. Y. Yamazaki, C.-K. Yang and S. M. Haile, *Scripta Mater.*, 2011, **65**, 102-107.
39. A. Navrotsky, *J. Mater. Chem.*, 2010, **20**, 10577.
40. J. Cheng and A. Navrotsky, *J. Solid State Chem.*, 2004, **177**, 126-133.
41. S. Buyukkilic, T. Shvareva and A. Navrotsky, *Solid State Ionics*, 2012, **227**, 17-22.
42. M. Aizenshtein, T. Y. Shvareva and A. Navrotsky, *J. Am. Ceram. Soc.*, 2010, **93**, 4142-4147.
43. W. Chen and A. Navrotsky, *J. Mater. Res.*, 2006, **21**, 3242-3251.
44. H. J. Avila-Paredes, T. Shvareva, W. Chen, A. Navrotsky and S. Kim, *Phys. Chem. Chem. Phys.*, 2009, **11**, 8580-8585.
45. E. R. Camargo, M. Popa, J. Frantti and M. Kakihana, *Chem. Mater.*, 2001, **13**, 3943-3948.
46. E. R. Camargo, M. G. Dancini and M. Kakihana, *J. Mater. Res.*, 2014, **29**, 131-138.
47. A. Navrotsky, *Phys Chem Minerals* 1997, **24**, 20.
48. A. Navrotsky, *J. Chem. Thermodyn.*, 2001, **33**, 859-871.
49. A. Navrotsky, *Phys. Chem. Miner.*, 1977, **2**, 89-104.
50. E. Fabbri, D. Pergolesi, S. Licoccia and E. Traversa, *Solid State Ionics*, 2010, **181**, 1043-1051.
51. S. Imashuku, T. Uda, Y. Nose and Y. Awakura, *J. Phase Equilibria Diffusion*, 2010, **31**, 348-356.
52. J. O. A. Paschoal, H. Kleykamp and F. Thümmler, *J. Nucl. Mater.*, 1987, **151**, 10-21.
53. R. Cervera, Y. Oyama, S. Miyoshi, K. Kobayashi, T. Yagi and S. Yamaguchi, *Solid State Ionics*, 2008, **179**, 236-242.
54. T. S. Hans G. Bohn, *J. Am. Ceram. Soc.*, 2000, **83**, 5.
55. S. B. C. Duval, P. Holtappels, U. Vogt, E. Pomjakushina, K. Conder, U. Stimming and T. Graule, *Solid State Ionics*, 2007, **178**, 1437-1441.
56. F. Iguchi, N. Sata and H. Yugami, *J. Mater. Chem.*, 2010, **20**, 6265.
57. V. M. Goldschmidt, *NATURWISSENSCHAFTEN* 1926, **14**, 477-485.
58. R. D. Shannon, *Acta Crystallogr. Sect. A: Found. Crystallogr.*, 1976, **32**, 751-767.

59. A. F. Sammells, R. L. Cook, J. H. White, J. J. Osborne and R. C. MacDuff, *Solid State Ionics* 1992, **52**, 111-123.

60. R. F. Schaufele, *J. Chem. Phys.*, 1967, **46**, 2859.

61. I. Charrier-Cougoulic, T. Pagnier and G. Lucazeau, *J. Solid State Chem.*, 1999, **142**, 220-227.

62. M. Karlsson, A. Matic, C. S. Knee, I. Ahmed, S. G. Eriksson and L. Börjesson, *Chem. Mater.*, 2008, **20**, 3480–3486.

63. A. Slodczyk, P. Colomban, S. Willemin, O. Lacroix and B. Sala, *J. Raman Spectroscopy*, 2009, **40**, 513-521.

64. A. Slodczyk, M.-H. Limage, P. Colomban, O. Zaafrani, F. Grasset, J. Loricourt and B. Sala, *J. Raman Spectroscopy*, 2011, **42**, 2089-2099.

65. R. A. Robie and B. S. Hemingway, *U.S. Geological Survey Bulletin*, 1995, **2131**.

66. A. V. Radha, O. Bomati-Miguel, S. V. Ushakov, A. Navrotsky and P. Tartaj, *J. Am. Ceram. Soc.*, 2009, **92**, 133-140.

67. P. Zhang, A. Navrotsky, B. Guo, I. Kennedy, A. N. Clark, C. Lesher and Q. Liu, *J. Phys. Chem. C*, 2008, **112**, 7.

68. E. Takayama-Muromachi and A. Navrotsky, *J. Solid State Chem.*, 1988, **72**, 244-256.

69. N. U. Navi, R. Z. Shneck, T. Y. Shvareva, G. Kimmel, J. Zabicky, M. H. Mintz, A. Navrotsky and C. Jantzen, *J. Am. Ceram. Soc.*, 2012, **95**, 1717-1726.

70. S. K. Sahu, P. S. Maram, A. Navrotsky and T. Vanderah, *J. Am. Ceram. Soc.*, 2013, **96**, 3670-3676.

71. P. Babilo, T. Uda and S. M. Haile, *J. Mater. Res.*, 2007, **22**.

72. J. Wu, S. M. Webb, S. Brennan and S. M. Haile, *J. Appl. Phys.*, 2005, **97**, 054101.

73. J. Wu, R. A. Davies, M. S. Islam and S. M. Haile, *Chem. Mater.*, 2005, **17**, 6.

74. D. Makovec, Z. Samardzija and D. Kolar, *J. Am. Ceram. Soc.*, 1997, **80**, 3145–3150.

75. J. Zhi, A. Chen, Y. Zhi, P. M. Vilarinho and J. L. Baptista, *J. Am. Ceram. Soc.*, 1999, **82**, 1345–1348.

76. S. Imashuku, T. Uda, Y. Nose and Y. Awakura, *J. Alloys Compd.*, 2010, **490**, 672-676.